Journal of Materials Chemistry A

ROYAL SOCIETY OF CHEMISTRY

PAPER

View Article Online
View Journal



Check for updates

Cite this: DOI: 10.1039/d5ta08480f

# Machine-learning-driven integrated probing of oxygen-vacancy distribution and ionomer morphology in an iridium oxide catalyst–ionomer nanocomposite electrode for water electrolyzers

Yerin Jeon, †[a] Sang-Hyeok Yang, †[a] Hyeon-Ah Ju, †[a] Kwanhong Park, †[b] Wooseon Choi, [a] Daehee Yang, [a] Hakjoo Lee, [c] Dami Lim, [c] Shin Jang, [c] Jaekwang Lee, *[b] Jae-Hyeok Kim *[c] and Young-Min Kim *[ad]

Tuning the oxygen vacancy ($V_o$) content and spatial distribution of the ionomer in $IrO_{2-x}$–ionomer nanocomposite electrodes is a crucial strategy for developing stable and efficient water electrolyzers. This underscores the necessity of developing a methodology capable of jointly mapping the $V_o$ and ionomer distributions with high spatial resolution. However, simultaneously visualizing and quantifying these two critical features in heterogeneous nanocomposite systems remains challenging. Exploiting the advantages of scanning probe-based electron energy-loss spectroscopy spectrum imaging (EELS SI) for identifying defect states and chemical phases on the nanoscale, we propose an efficient machine-learning-driven electron spectroscopic method for mapping the $V_o$ and ionomer distributions over $IrO_{2-x}$–ionomer nanocomposites at high resolution. Integrating spectroscopic imaging and machine learning offers a novel solution for disentangling overlapping spectral features in complex nanocomposites. Based on the high-throughput data processing of large EELS SI datasets, our approach allows statistical assessment of the degrees of $V_o$ homogeneity and ionomer coverage in the $IrO_{2-x}$–ionomer composite electrode. We found that the local $V_o$ concentrations are closely related to the degree of local ionomer coverage over the $IrO_{2-x}$ catalyst particles. This suggests that the surface charge density altered by $V_o$ directly affects the electrostatic interactions governing ionomer adsorption. Because this machine-learning-driven EELS SI method is optimized for grouping and classifying C K- and O K-edges from unsupervised classes, it can be widely used as an efficient tool for characterizing the $V_o$ distribution and differentiating carbon-based chemical phases in various vacancy-tailored oxide catalyst–ion-conducting polymer electrodes.

Received 18th October 2025
Accepted 14th April 2026

DOI: 10.1039/d5ta08480f

rsc.li/materials-a

## Introduction

In the development of high-performance proton-exchange membrane water electrolyzers (PEMWEs) that split water into hydrogen and oxygen using electricity, iridium oxide ($IrO_2$) is considered one of the most active catalysts and remains stable under acidic conditions in the oxygen evolution reaction (OER).[1,2] Continuous research efforts have been dedicated to improving the slow kinetics of the OER and sluggish material transport within catalyst-coated membranes (CCMs), which present significant challenges for the efficient operation of PEMWEs.[3,4] To achieve higher hydrogen production rates, enhancing the OER activity of $IrO_2$ catalysts (or Ir-based alloys/compounds) is an issue that needs to be addressed, as commercialized PEMWEs still require substantial use of Ir-based OER catalysts.[5–7] As the OER performance of $IrO_2$-based nanomaterials is closely tied to the surface atomic arrangements and related defect densities therein,[7–11] modifying the surface/interface atomic arrangements and controlling the atomic defect concentrations while maintaining their lattice structures have been adopted as effective strategies for tailoring electronic configurations to improve catalytic performance.[12–21]

When oxygen vacancies ($V_o$) are created within $IrO_2$, resulting in $IrO_{2-x}$, the overpotential for the acidic OER can be reduced by modulating the Ir d orbital states, which is favorable for enhancing the OER performance.[20,22,23] Thus, balancing the $V_o$ content and lattice structure stability of $IrO_{2-x}$ provides

[a]Department of Energy Science, Sungkyunkwan University (SKKU), Suwon 16419, Republic of Korea. E-mail: youngmk@skku.edu

[b]Department of Physics, Pusan National University, Busan 46241, Republic of Korea. E-mail: jaekwangl@pusan.ac.kr

[c]Water Electrolyzer Engineering Design Team, Hyundai Motor Company, Yongin 16891, Republic of Korea. E-mail: jhkim3@hyundai.com

[d]Center for 2D Quantum Heterostructures, Institute for Basic Science (IBS), Suwon 16419, Republic of Korea

† Y. J., S.-H. Y., H.-A. J., and K. P. contributed equally to this study.

insight into the $V_o$-mediated charge–lattice coupling effect and relevant electronic structure reconfiguration,[20,24–26] helping to establish strategies for developing more active and durable catalytic materials with reduced use of noble metals, such as Ir. The anode layer in the PEMWE is a composite of $IrO_{2-x}$ and an ionomer with a porous morphology.[27] An ionomer is a specialized polymer that conducts ions while maintaining its structural integrity, thanks to ionic functional groups attached to the polymer backbone chain. In the use of the catalyst inks of $IrO_{2-x}$ blended with an ionomer (Nafion® in this case) to prepare membrane electrode assemblies (MEAs) of PEMWEs *via* the CCM method, the morphological distribution of the ionomer, describing how it coats the catalyst particles, is a crucial parameter in optimizing the electrochemical performance of PEMWE electrodes.[28–31] Thus, the morphology of ionomers decorating $IrO_{2-x}$ catalytic particles must be visualized and measured for efficient interface engineering of the $IrO_{2-x}$ catalyst–ionomer composite.[32]

(Scanning) transmission electron microscopy ((S)TEM) accurately captures not only the atomic arrangement (crystal structure) of metal-oxide catalysts such as $IrO_{2-x}$ nanoparticles but also their morphological distribution with high precision.[13,17,33] However, this imaging method is typically unable to detect oxygen vacancies within the $IrO_2$ crystal lattice, and simultaneously imaging carbon-based ionomers and catalyst particles is challenging because of the relatively weak scattering of the ionomer under an electron beam. In this respect, nanoscale electron energy-loss spectroscopy (EELS) mapping of the O K- and C K-edges can be an alternative analytical method. However, EELS spectrum imaging (SI) analysis based on a few samples raises questions regarding the statistical significance of the results despite providing high-resolution information on the nanoscale phase distribution of the sample. Furthermore, conventional digital fitting using the multiple linear least squares (MLLS) algorithm to interpret EELS SI data can often misclassify the spatial distributions of chemical phases because it relies on high-quality references and sensitivity to experimental conditions.[34,35]

Hence, a reference-free data processing approach based on a large EELS SI dataset must be established to address these concerns. From an experimental viewpoint, radiolytic damage to a sample is another concern because prolonged electron-beam irradiation is required to acquire interpretable chemical mapping data.[36] This unfavorable damage phenomenon can cause the artificial generation of oxygen vacancies inside the $IrO_{2-x}$ nanoparticles and mass loss (or morphological distortion) of ionomers, leading to misleading interpretations. Therefore, an appropriate experimental strategy must be devised to prevent unwanted sample damage and ensure measurement accuracy.

In this study, we propose a machine-learning-driven chemical-mapping method based on a large EELS SI dataset of O K- and C K-edges to probe the morphological distributions of $V_o$ and ionomers in $IrO_{2-x}$ catalyst–ionomer composite electrodes with statistical significance. Using the machine-learning capability of reference-free clustering of the EELS spectra with contextual relationships, two distinctive phases of $IrO_{2-x}$ with $V_o$ and an ionomer decorating the catalyst particles in the electrode were reliably visualized. As the O K-edge profile is sensitive to the degree of $V_o$ concentration,[12,16,25,37,38] a series of O K EELS spectra were simulated using density functional theory (DFT) calculations to examine the variation of the O K-edge shape as a function of the $V_o$ content in the $IrO_{2-x}$ structure. The results indicated that the intensity ratio of $t_{2g}$ to $e_g$ peaks gradually decreased from the reference state of stoichiometric $IrO_2$ as the $V_o$ content increased. This decreasing trend in the $t_{2g}/e_g$ peak ratio was used as a scaling curve to obtain a $V_o$ distribution map from the experimentally measured $t_{2g}/e_g$ peak ratios for all the O K spectra. In parallel, machine-learning clustering of the C K-edges was conducted to determine how the ionomers decorated the $IrO_{2-x}$ catalyst particles. By applying the two parallel machine-learning agents for interpreting O K- and C K-edges to a large EELS SI dataset, a statistically meaningful analysis of the $V_o$ distribution in the $IrO_{2-x}$ catalyst particles and the morphological distribution of ionomers was achieved without human bias in data interpretation. This machine-perspective EELS SI data processing technique can clarify the effects of the vacancy distribution inside the catalysts and the interfacial morphology of ionomers on water electrolysis properties, which are vital for the efficient engineering of high-performance OER electrodes.

# Experimental

### Fabrication of the iridium oxide–ionomer composite electrode

Rutile iridium(IV) oxide (043 396, Alfa Aesar) was used as the electrocatalyst. The catalyst ink was prepared by dispersing the catalyst in a 1 : 1 (w/w) mixture of water and 1-propanol, followed by the addition of a Nafion dispersion (D2021) to achieve an ionomer-to-catalyst (I/C) weight ratio of 0.2. The slurry was ultrasonicated for 15 min, mixed, and homogenized *via* magnetic stirring at 400 rpm for 30 min. After mixing, the catalyst layer was coated onto a polyethylene naphthalate substrate using an adjustable film applicator. The catalyst layer was dried in an oven at 80 °C for 2 h.

### TEM sampling and EELS SI experiment

To prepare TEM samples for STEM EELS analysis, $IrO_{2-x}$ catalyst–ionomer composite samples were dispersed in deionized water *via* bath sonication and drop-cast onto lacey carbon support or graphene/lacey carbon support TEM grids, followed by drying at 60 °C. The morphologies and atomic structures of the prepared samples were analyzed in the annular dark-field (ADF) STEM imaging mode using an aberration-corrected transmission electron microscope (JEM-ARM200CF, JEOL Ltd) operating at 80 or 200 kV with a probe current of 40 pA. For ADF STEM imaging, the collection-angle range of the ADF detector was set to 45–180 mrad, and the probe convergence semi-angle was ~24 mrad. Core-loss EELS SI datasets for chemical mapping of the C K-edge and O K-edge were simultaneously acquired in the same sample regions in the ADF STEM mode using a GIF Quantum ER 965 spectrometer (Gatan, Inc.). The SI

 

acquisition was conducted with a scan step size of 3 nm per pixel, a dwell time of 0.5 s per pixel, and an energy dispersion of 0.1 eV per channel. The mapping resolution of the SI was set to 50 × 50 pixels, corresponding to a field of view of 150 × 150 $nm^2$.

### DFT calculations and O K EELS simulations

The calculations were performed using DFT within the projector-augmented wave (PAW) formalism,[39] as implemented in the Vienna *Ab initio* Simulation Package (VASP).[40] The exchange–correlation effects were treated using PBEsol functionals.[41] The plane-wave energy cutoff was set to 400 eV. A (110) slab model containing 60 Ir and 120 O atoms was used. The slab consisted of five atomic layers and a vacuum region of approximately 10 Å in the *z*-direction. The bottom three layers were fixed, whereas the top two layers were allowed to relax. All structural relaxations were performed with an energy-convergence criterion of $10^{-6}$ eV/cell and force convergence of $10^{-2}$ eV $Å^{-1}$. A Gamma-centered 1 × 1 × 1 *k*-point mesh was used for relaxation, and a 2 × 2 × 1 mesh with the tetrahedron method[42] was used for density of states calculations. To further ensure that the theoretical results are reliable and quantitatively meaningful, we performed additional DOS calculations using higher cutoff energies of 450 and 500 eV, and the results are provided in the SI (Fig. S1). The overall DOS features remain essentially unchanged compared to those obtained at 400 eV, supporting the qualitative robustness of our conclusions. To obtain the O K near-edge structure spectra of defective $IrO_{2-x}$, the surface oxygen atoms were systematically removed in pairs to generate a series of configurations ranging from $Ir_{60}O_{120}$ to $Ir_{60}O_{108}$ slabs. O K-edge simulations were performed by calculating the dielectric function using the supercell core–hole method.[43] The imaginary part of the dielectric function in the long wavelength limit ($q = 0$) is proportional to the absorption intensity.

$$\varepsilon_{\alpha\beta}{}^2(\omega) = \frac{4\pi^2 e^2 \hbar^4}{\Omega\omega^2 m_e{}^2} \sum_{c,k} 2\omega_k \delta(\varepsilon_{ck} - \varepsilon_{core} - \omega) \times M_\alpha^{\text{core}\to ck} M_\beta^{\text{core}\to ck*}$$

### EELS SI data processing using machine learning

To process the experimental C K EELS SI dataset using machine-learning algorithms, the energy-loss window was set to 270–330 eV to isolate the C K-edge region after removing irrelevant spectral regions, which increased the processing efficiency and accuracy. Additionally, stride binning by a factor of two was applied along the spatial dimensions to reduce data volume and enhance signal quality. The machine-learning workflow for C K EELS of ionomer mapping consists of two main steps: dimensionality reduction and clustering. For dimensionality reduction, non-negative matrix factorization (NMF) was applied to decompose the data into additive and non-negative components, which are suitable for the physical interpretability of spectral data.[44] The decomposed components were subjected to K-means clustering to partition the spatially correlated spectral feature components. Among the grouped spectral components, the spectral feature components of $k \leq 3$ were selected because the first three components reflected the physically meaningful morphologies of the $IrO_{2-x}$ catalyst particles, ionomers, and graphene overlayer of the TEM sample. NMF was initialized using the non-negative double singular value decomposition (NNDSVD) method, and convergence was monitored *via* the Frobenius norm of the residual matrix with a relative tolerance of $10^{-4}$ and a maximum of 20 000 iterations. For K-means clustering, k-means++ initialization was employed with ten independent restarts ($n_{\text{init}} = 10$) and an absolute tolerance of $10^{-4}$ over a maximum of 1000 iterations to confirm cluster stability. Subsequently, segmentation maps of the three components were generated *via* binarization to evaluate their areal distributions. Background subtraction is generally applied before subsequent data interpretation as a preprocessing treatment for EELS SI data. However, background subtraction was not implemented in this case, because the most abundant feature (or variance) regarding the overall particle morphology was lost (Fig. S2). Specifically, power-law background subtraction redistributed the pre-edge spectral intensity and reduced the weight of the morphological variance, causing the first-ranked NMF component to no longer correspond to the overall particle shape and displacing the ionomer-associated component to a physically irrelevant position (Fig. S2b). Retaining the background-inclusive data, therefore, preserved the hierarchical ordering of the three principal chemical phases necessary for reliable ionomer identification.

To analyze the O K EELS SI dataset, 2 × 2 stride binning was applied to reduce the data volume and enhance the signal quality. Subsequently, principal component analysis (PCA) was employed to denoise the spectral data by truncating high-order spectral components ($k \geq 4$ in this case) from the binned EELS SI dataset, after confirming that the reconstructed data preserved the key spectral features of the ionomer and graphene components. Background subtraction was performed by fitting the pre-edge region to a power-law model using linear regression. Background fitting was performed over a user-defined energy window ($\Delta E = 28$ eV) at 3 eV, preceding the onset (532 eV) of the O K-edge. The resulting fit was then extrapolated and subtracted from the entire spectrum to isolate edge-related signals. To facilitate accurate identification of the A and B peaks, which correspond to transitions into the unoccupied $t_{2g}$ and $e_g$ states of the metal–oxygen coordination environments, respectively, the spectra were smoothed using the Savitzky–Golay filtering algorithm with a window length of 21 and polynomial order of 2. In this process, peak B is defined as the global maximum within the post-edge region, whereas peak A is identified as a local maximum or saddle point in the pre-B region, where the absolute value of the first derivative reaches a local minimum. This derivative-based fitting approach allows consistent and reproducible estimation of the A/B intensity ratio,[16,22] facilitating further comparison and interpretation.

All spectral data were collected exclusively from $IrO_{2-x}$–ionomer composite samples prepared in-house; no external datasets were used. Each SI dataset comprised 50 × 50 spatial pixels with simultaneous C K- and O K-edge spectra at each position, yielding approximately 175 000 spectra per ionization edge across the full ensemble of more than 70 datasets. Since NMF, PCA, and K-means are unsupervised algorithms that operate

directly on experimental spectra without labelled examples, conventional training/testing split procedures are not applicable. The performance is instead evaluated by the physical interpretability of the decomposed components and the spatial coherence of the resulting maps. The machine-learning workflow for this study was designed using the Python-based Scikit-learn library, and the source code is available on GitHub (https://github.com/SKKU-STEM/ESICharWE).

## Results and discussion

### Microstructure and spectroscopic characterization of the $IrO_{2-x}$–ionomer composite

The typical morphology of the $IrO_{2-x}$–ionomer composite prepared for TEM analysis is shown in Fig. 1a. An ADF STEM image captured at low magnification revealed that the iridate particles in the composite were severely agglomerated, exhibiting a wide range of sizes from several nanometers to approximately 80 nm. Interestingly, statistical measurement revealed that the sizes of the $IrO_{2-x}$ particles exhibit a bimodal distribution, with distinctive sizes of 6.8 ± 4.8 and 15.8 ± 15.2 nm (Fig. S3). A weak contrast appearing around the edges of the agglomerated particles indicated the presence of an ionomer decorating the iridate particles (see the arrow denoting the ionomer part). However, obtaining a holistic view of the mixing of conducting ionomers with iridate catalyst particles is challenging. In particular, the difficulty of discernibility worsens when the sample is on a carbon support. Atomic-scale ADF STEM imaging of the iridate particles oriented in the [011] and [131] directions indicated that the crystal structure was rutile, and the atomic models of the rutile lattices with these orientations confirmed the STEM observations (Fig. 1b and c). To distinguish the ionomer component from carbon, the spectral features of the C K-edge profile were examined using EELS, because the near-edge structure of the C K-edge is sensitive to chemical phases with different bonding attributes of carbon-based compounds or composites. In a recent study, the C K-edge profile of an ionomer exhibited a characteristic spectral peak at ~288 eV, corresponding to the C 1s–π* transition associated with C=O or C–OH bonds in ionomer polymeric chains.[45] This peak is distinguished from π* and σ* peaks (denoted by C1 and C3, respectively), which are mainly associated with C=C $sp^2$ and C–C $sp^3$ bonds, originating from the C-support and graphene protection overlayer. Indeed, we observed a characteristic peak at approximately 288 eV in the C K-edge profile obtained for the ionomer part of the composite sample (denoted as C2 in Fig. 1d). Thus, the distinguished C2 peak at ~288 eV can be used as a characteristic spectral signature to probe the ionomer morphology in the composite sample. To map the ionomer distribution in $IrO_{2-x}$–ionomer composites, MLLS fitting is typically used because it can differentiate the local distribution of different chemical phases from the

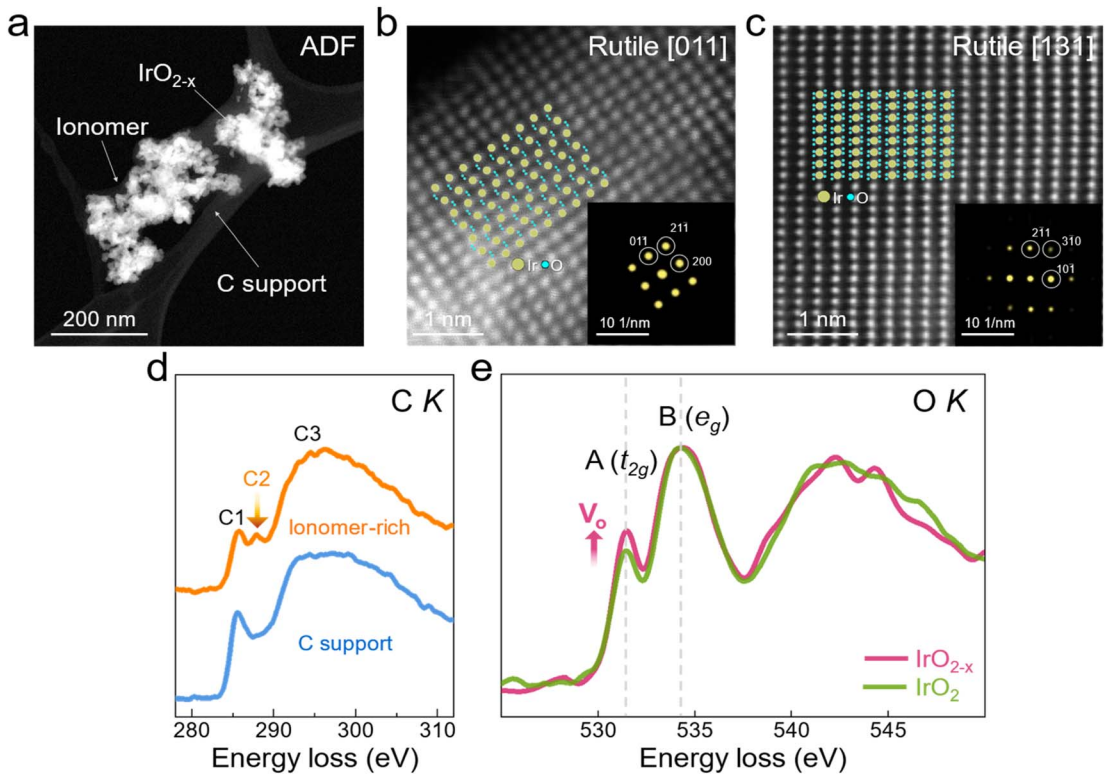


Fig. 1 Typical structural and chemical features of the $IrO_{2-x}$–ionomer composite for the PEMWE electrode. (a) Low-magnification ADF STEM image of the $IrO_{2-x}$–ionomer composite sample supported on a C-support TEM grid. (b and c) Atomic-scale ADF STEM images of the rutile $IrO_{2-x}$ nanoparticles aligned to the [011] and [131] orientations. (d) Comparison of O K EELS spectra obtained from ionomer and C-support regions. (e) Comparison of O K EELS spectra obtained from O-deficient $IrO_{2-x}$ and stoichiometric $IrO_2$ particles in the sample.

 

EELS SI data.[46,47] In this fitting process, the local phase spectra are represented as components with distinct linear coefficients, and the total spectrum is obtained by a linear combination of the local spectra. Hence, this method requires manually assigned reference components for linear fitting to obtain fit-coefficient maps. Given this requirement for manual input, the fidelity of the method is often not guaranteed, because the fitting results depend on the selected position-specific reference spectra, and the output data become unreliable when the difference among the local component spectra is subtle, as in the case of the C K-edge of the ionomer (Fig. S4). Machine-perspective data processing can be a solution to avoid data distortion caused by human bias when selecting reference spectral components.

In rutile $IrO_2$, six oxygen atoms are coordinated around the iridium cation, creating $IrO_6$ octahedral channels along the *c*-axis. The octahedral crystal field splits the Ir 5d orbitals into lower-energy ($t_{2g}$) and higher-energy ($e_g$) bands, resulting in a partially filled band in the $t_{2g}$ orbitals, which is considered the fundamental basis for its intrinsic metallic conductivity.[48] When a $V_o$ is created in the lattice, the Ir cations become unsaturated, leading to local distortions in the bond configuration, which result in different geometric and electronic environments. Thus, the increased number of undercoordinated sites with increasing $V_o$ content imposes the combined effects of electronic perturbations and geometric changes, which typically act as loci for improved catalytic activity.[49] Despite the benefits of improving catalytic performance, the catalytic activity and stability of iridium oxide in acidic media often exhibit an inverse relationship, and rutile $IrO_2$ is degraded during the OER.[50,51] Furthermore, the lattice oxygen in rutile $IrO_2$ participates in the dynamic exchange process under various OER conditions.[50] Therefore, a method that can reliably visualize and monitor the formation and annihilation of $V_o$ during the OER is needed to evaluate the effects of $V_o$ on the catalytic performance and stability of oxide catalysts. To probe the $V_o$ distribution in the $IrO_{2-x}$ catalyst particles, the O K-edge profiles of the stoichiometric and oxygen-deficient iridate catalysts were compared, because the O K EELS spectrum reveals the electronic structure of the hybridized O 2p–Ir 5d$t_{2g}$ and $e_g$ orbitals in $IrO_2$ and its profile sensitively changes in response to the $V_o$ content in the lattice.[12,52] Moreover, it delivers distinguishable information on the atomic structures of amorphous and hollandite-type $IrO_x$ and rutile-type $IrO_2$ phases because they have different orbital hybridization profiles at the O K-edge.[53] Fig. 1e shows the experimental O K-edge profiles of stoichiometric $IrO_2$ and oxygen-deficient $IrO_{2-x}$. The experimental O K EELS spectra of the two samples exhibit a characteristic doublet profile featured by peaks A (~531.3 eV) and B (~534.4 eV) with an energy difference of ~3 eV, which stems from the transition to hybridized empty states of 2p–Ir 5d$t_{2g}$ and $e_g$ orbitals. The results indicate that peak A (associated with $t_{2g}$ orbitals) of the oxygen-deficient $IrO_{2-x}$ was higher than that of the reference $IrO_2$, resulting in an increase in the A/B ratio. The increased intensity of peak A originates from the fact that the two electrons associated with the neutral $V_o$ can contribute to the conduction band or localize to adjacent Ir sites, increasing the density of states near the Fermi level. This result suggests that we can obtain useful information on the distribution of $V_o$ over the $IrO_{2-x}$ catalyst particles by measuring and mapping the A/B ratios of site-specific O K-edges over the sample.

To investigate how the A/B ratio in the O K-edge fine structure of $IrO_2$ responds to varying $V_o$ concentrations, we performed DFT simulations using a series of slab models with progressively reduced oxygen contents, ranging from stoichiometric $Ir_{60}O_{120}$ to $Ir_{60}O_{108}$ (corresponding to 10% oxygen deficiency) (Fig. 2). Surface oxygen atoms were systematically removed in pairs to generate these configurations, as illustrated in Fig. 2a (left). The density of states was calculated for

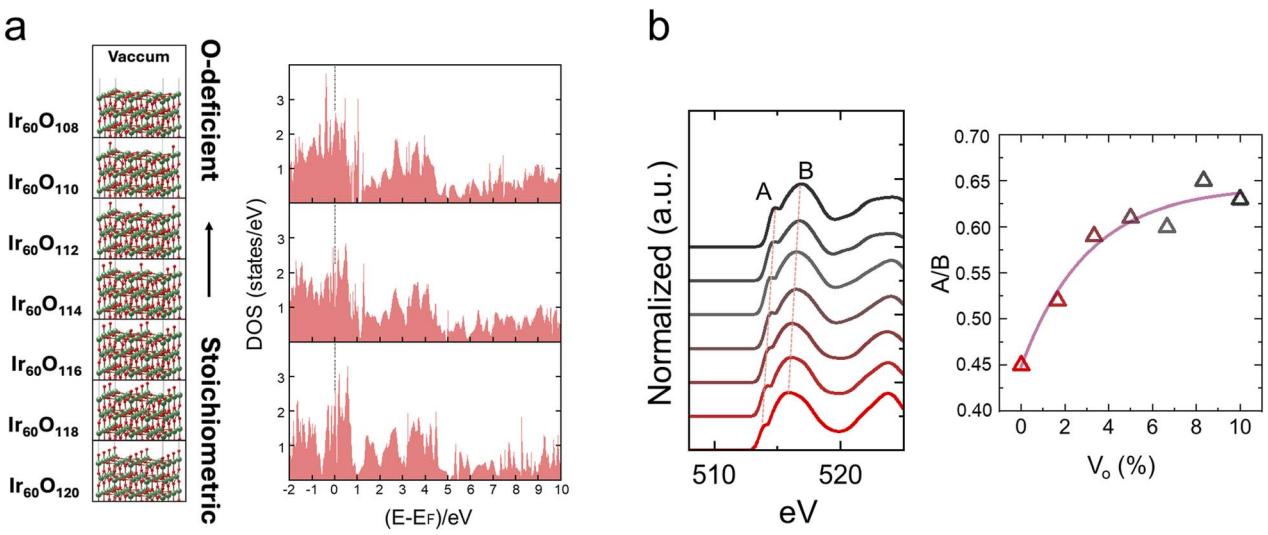


Fig. 2 DFT modeling of oxygen-deficient defective $IrO_{2-2x}$ and O K-edge simulations. (a) (left) Atomic structures illustrating increasing oxygen vacancy concentration ($V_o$), from stoichiometric $IrO_2$ to defective $IrO_{2-2x}$ ($x = 0.1$), and (right) the density of states for stoichiometric $IrO_2$, $IrO_{2-2x}$ with $x = 0.02$ (2% $V_o$), and $x = 0.1$ (10% $V_o$). (b) (left) Normalized O K-edge spectra for $IrO_{2-2x}$ with varying $V_o$ concentration. (right) The A/B intensity ratio as a function of $V_o$ concentration. Green and red spheres denote Ir and O atoms, respectively.

stoichiometric $IrO_2$ and oxygen-deficient $IrO_{2-2x}$ with $x = 0.02$ (2% $V_o$), and $x = 0.1$ (10% $V_o$), as shown in Fig. 2a (right). The pristine $IrO_2$ (110) slab exhibited metallic behavior, which persisted across all $V_o$ concentrations. From the O K-edge simulations of the defective $IrO_{2-2x}$, the most distinct spectral evolution was a gradual increase (Fig. 2b (right)) and eventual saturation of the A/B peak intensity ratio with increasing $V_o$ content (Fig. 2b (left)), which was used to scale the measured A/B ratio map to the $V_o$ distribution map. The energy separation between peaks A and B ($\Delta E_{B-A}$) remains constant at approximately 2.1 eV across the entire range of oxygen vacancy concentrations (Fig. 2b (left)).

### Scheme of machine-learning-driven EELS SI characterization

To address the need to establish an efficient methodology for simultaneously probing the $V_o$ content in $IrO_{2-x}$ catalyst particles and the morphological distribution of decorated ionomers, we employed two independent machine-learning agents combined for parallel data processing of the EELS SI dataset of O K- and C K-edges. The EELS SI dataset was acquired in the form of a 3D data cube in which every pixel in a 2D STEM image of the sample contained a position-specific 1D spectrum. The workflow of our machine-learning-driven process is shown in Fig. 3 and consists of three steps. First, the experimentally acquired EELS SI dataset for the $IrO_{2-x}$–ionomer composite sample was preprocessed *via* plural scattering deconvolution to remove the thickness-dependent multiple scattering effect, whereby thickness variations over the agglomerated particles induced artificial changes in the O K- and C K-edge intensities regardless of the actual content. A numerical treatment using min–max normalization was applied to the deconvoluted O K- and C K-edge signal components to prepare them for machine-learning data processing.

For the morphological distribution analysis of ionomers using C K EELS SI data, NMF[44] and K-means clustering[54] were employed to redistribute all the position-registered C K-edges into a low-dimensional latent space and group similar C K-edges, which were determined by the Euclidean distances

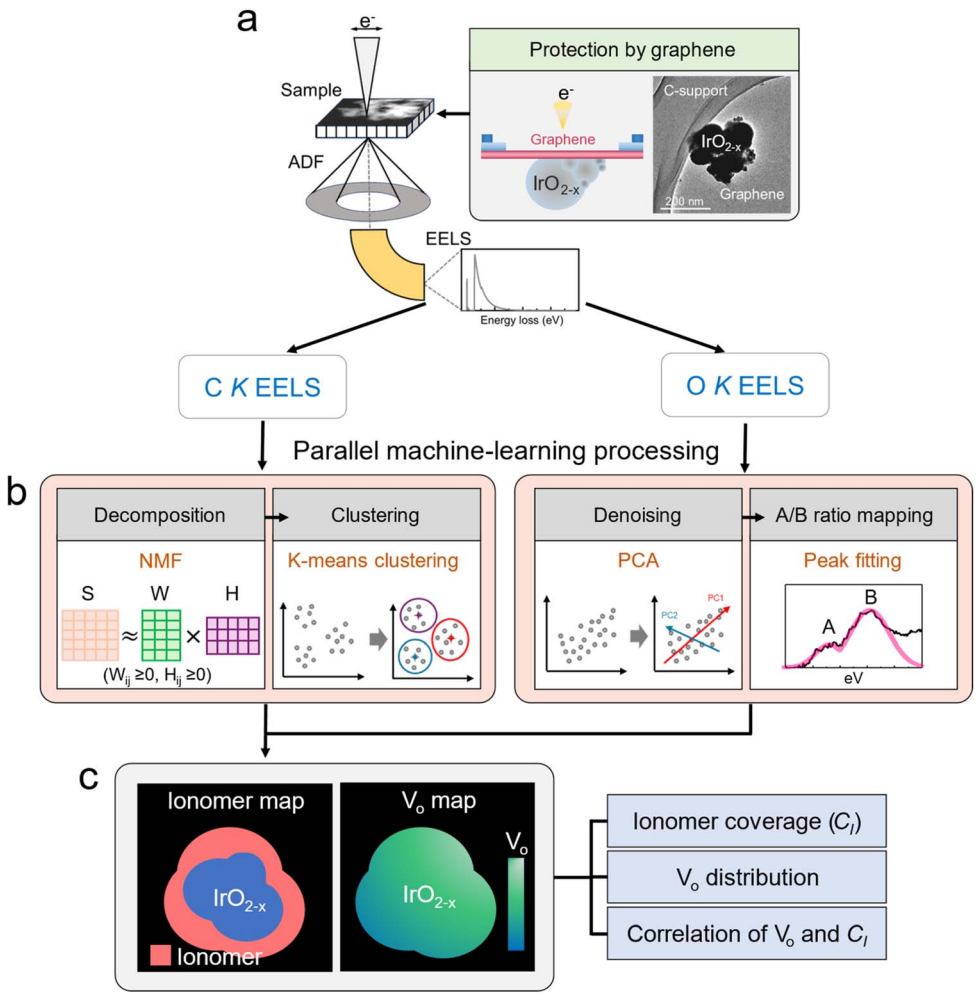


Fig. 3 Concept of a three-step workflow for machine-learning-driven analysis of the O K and C K EELS SI dataset of the $IrO_{2-x}$–ionomer composite electrode. (a) Step 1: experimental acquisition and preprocessing of the C K and O K EELS SI datasets. (b) Step 2: parallel machine-learning data processing for individual C K and O K EELS SI datasets with different processing algorithms. (c) Step 3: generation of the composite map of ionomer and $V_o$ distributions over the sample, allowing statistical evaluation of the ionomer coverage, $V_o$ concentration gradient, and geometric two-parameter correlation.

 

among the spectral features scattered into a low-dimensional space. Because NMF is capable of extracting contextually related spectral features from multidimensional EELS SI data with non-negative constraints,[33,55] NMF-based feature classification can precisely discriminate individual spectra in EELS SI data with the complexity of overlapping or proximity in the real space of observation. We expected the following K-means clustering to provide the advantages of increased accuracy in identifying the spatial distribution of the ionomer phase and enhanced interpretability of the results in the EELS SI analysis of $IrO_{2-x}$–ionomer samples. This is because categorized clusters are associated with different regions or chemical phases in the sample, and physically meaningless clusters, such as noisy spectral data, can be ruled out during the process. Furthermore, this clustering process is relatively simple and computationally efficient, making it suitable for analyzing large EELS SI datasets for statistical evaluation.

In contrast to the C K-edges exhibiting different spectral profiles between the ionomer and carbon support, the shape difference in the O K-edges of many oxides with or without $V_o$ is usually insignificant because the $V_o$ content in oxides is small, at the level of a few percent. On the other hand, the relative $t_{2g}$/$e_g$ peak ratio in the O K-edge profile is sensitive to changes in the $V_o$ content.[12,13,56] Thus, precise measurement of the subtle variations in the peak ratio across all O K-edge spectra is crucial for probing the $V_o$ distribution in oxide samples. This requires a high-quality O K-edge with the splitting of the $t_{2g}$/$e_g$ doublet for reliable measurement. To this end, we utilized a PCA algorithm to remove the low-variance components of physically meaningless spectral features from the experimental EELS SI data of the O K-edge, thereby increasing the signal-to-noise ratio of the O K-edges. After the denoising process, we applied Gaussian fitting to extract $t_{2g}$ and $e_g$ (hereinafter denoted as A and B, respectively) peaks from all the denoised O K-edge spectra of the EELS SI, subsequently obtaining an A/B ratio map. Note that the power-law-dependent backgrounds should be subtracted from the input O K EELS SI data to make the Gaussian fitting more reliable, which is a different requirement for input data preparation from the case of C K EELS SI. We also prepared a scaling curve describing the change in the A/B ratio as a function of the $V_o$ content *via* systematic DFT modeling. Using this scaling curve, the A/B ratio map was converted into a $V_o$ distribution map *via* a code-based computation routine. In the last step, we generated a combined map of the two-phase areal distribution of the $IrO_{2-x}$–ionomer and the $V_o$ distribution in the $IrO_{2-x}$ nanoparticles. The obtained composite map simultaneously visualizes the morphological distribution of the ionomers on the $IrO_{2-x}$ catalysts and the extent to which $V_o$ is populated. Moreover, automated data processing for a large EELS SI dataset of the $IrO_{2-x}$–ionomer composite sample allowed the evaluation of the ionomer coverage, $V_o$ concentration gradient, and geometric two-parameter correlation with statistical significance. This information enabled us to obtain valuable data-driven insights into establishing a reliable testbed for composite materials and an engineering strategy for developing high-performance catalytic electrodes for PEMWEs.

**Electron-beam-induced damage-free EELS SI data acquisition**

Iridium oxides suffer from electron-beam-induced damage due to knock-on displacement or radiolysis caused by high-energy electron-beam irradiation.[57] The pristine lattice structure of iridium oxide is readily reduced to iridium metal because of the knock-on effect, whereby oxygen atoms are physically sputtered from the lattice. This unfavorable effect can be mitigated by reducing direct momentum transfer to the atoms when the accelerating voltage of the electron beam is lowered. Nonetheless, the radiolytic bond breakage arising from the ionization of bonding electrons can drive oxygen loss in the rutile lattice, leading to the artificial generation of oxygen vacancies. Indeed, when the $IrO_{2-x}$ sample was exposed to a 200 kV electron beam, oxygen vacancies were immediately generated at a high rate (Fig. 4a and the green curve in Fig. 4d), and rutile $IrO_{2-x}$ was subsequently reduced to iridium metal (Fig. S5). By reducing the accelerating voltage to 80 kV, the threshold time to trigger radiolysis-induced vacancy generation was extended to ~127 s at the same dose rate of $2.78 \times 10^7$ $e^- s^{-1} nm^{-2}$ (Fig. 4b and the light blue curve in Fig. 4d). However, this endurance to electron-beam irradiation is insufficient for obtaining damage-free STEM SI datasets of the C K- and O K-edges of the $IrO_{2-x}$–ionomer composite sample, because obtaining a STEM SI dataset requires >20 min for this acquisition condition, which corresponds to a total electron dose of $3.43 \times 10^{10}$ $e^-/nm.^2$

To address this issue, we utilized a graphene-supported TEM grid for sample preparation. Graphene overlayers with high in-plane thermal and electrical conductivities are known to confer effective protection against electron-beam-induced damage in oxide catalysts and other nanomaterials.[58,59] The primary protective mechanism is charge dissipation. Prolonged electron irradiation accumulates electrostatic charge on the relatively insulating $IrO_{2-x}$ and ionomer surfaces, which lowers the activation barrier for radiolytic bond breakage. Graphene, as a highly conductive two-dimensional material, provides a lateral current pathway that efficiently drains the accumulated charge, thereby suppressing radiolysis-driven damage. A secondary contribution arises from thermal conduction, as the exceptionally high in-plane thermal conductivity of the graphene facilitates rapid lateral dissipation of locally deposited beam energy, thereby suppressing thermally activated oxygen loss. Indeed, when our sample was protected by a graphene overlayer, as shown in Fig. 4c, it exhibited a notably higher resistance to radiation damage, approximately 10-fold greater than that of the case without the graphene overlayer. Generally, the degree of the radiation-induced loss of oxygen atoms from $IrO_{2-x}$ particles depends on their size; smaller particles correspond to greater loss of oxygen atoms. During the serial acquisition of the O K EELS SI, noticeable loss of oxygen atoms was observed for particles smaller than 5 nm in the bare $IrO_{2-x}$ sample, resulting in an artificially increased vacancy concentration (red arrows in Fig. 4e). In contrast, the small $IrO_{2-x}$ nanoparticles in the graphene-protected $IrO_{2-x}$ sample remained intact even under prolonged electron-beam irradiation (Fig. 4f). Using this preparation method, we obtained all the STEM SI datasets for the $IrO_{2-x}$ samples under pristine conditions.

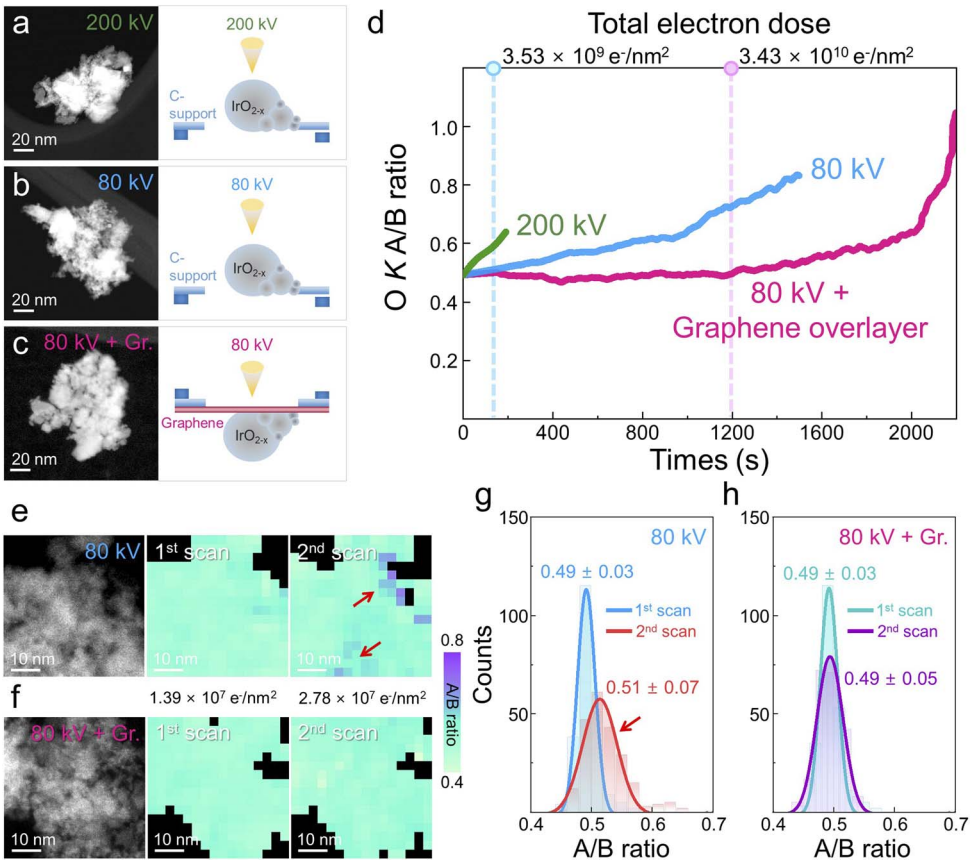


Fig. 4 Examination of electron-beam-induced oxygen-vacancy generation. (a–c) Morphologies of three $IrO_{2-x}$ samples prepared using a lacey carbon support and graphene overlayer, which were observed under accelerating voltages of 200 and 80 kV, respectively. The leftmost figures schematically describe the TEM samples prepared for STEM EELS SI analysis. (d) Profiles showing the temporal changes of A/B peak ratios in O K EELS spectra of the $IrO_{2-x}$ TEM samples under electron beams accelerated at 200 or 80 kV at the dose rate of $2.78 \times 10^7$ $e^-$ $s^{-1}$ $nm^{-2}$. (e and f) First two consecutively acquired A/B ratio maps for the bare $IrO_{2-x}$ and the $IrO_{2-x}$ protected by the graphene overlayer, respectively. (g and h) Comparison of the histograms of the A/B peak ratios between the first and second acquisitions of the O K EELS SI for the bare $IrO_{2-x}$ and the graphene-protected $IrO_{2-x}$ particles. Note that the A/B ratio of the bare $IrO_{2-x}$ was increased after the second acquisition, whereas the one protected by the graphene overlayer remained almost unchanged.

### Machine-learning-driven mapping of ionomer distribution and $V_o$ gradient

The C2 peak observed at ~288 eV at the C K-edge was a key spectral feature for discriminating the ionomer from the carbon support and graphene overlayer in the TEM grid sample, as shown in Fig. 1d. As the STEM EELS SI data consist of a hyperspectral cube ($x$, $y$, energy loss), where each pixel in the SI contains a spatially correlated EELS spectrum, this 3D dataset must be unfolded into a 2D matrix ($S$) with dimensions of $N_{x,y} \times E_c$ for mathematical manipulation using machine learning, where $N_{x,y}$ represents the total number of spatial pixels and $E_c$ represents the number of energy-loss channels. The NMF algorithm was then used to decompose the 2D spectral data matrix ($S$) into a product of two lower-dimensional matrices ($S \approx WH$): the location-specific coefficient matrix ($W = N_{x,y} \times k$) and spectral feature components ($H = k \times E_c$), where $k$ represents the number of classified spectral components (Fig. 5a). After the iterative optimization, the order of $k$ reflects the rank of its contribution to the total spectral variance, where the first component exhibits the greatest variance across the energy range.

Fig. 5a (top panels) shows the first three coefficient maps decomposed using NMF. The first-ranked coefficient map ($k = 1$) represents the morphological distribution of the $IrO_{2-x}$ catalyst particles because the agglomerated $IrO_{2-x}$ particles manifest as an overall morphological feature with varying thicknesses in the composite sample. On the other hand, the third-ranked coefficient map represents the morphology of the ionomer, whereas the second-ranked coefficient map shows the total distribution of carbon including the graphene overlayer. The associated spectral feature component profiles for $k \leq 3$ correspond to these sorted coefficient images, confirming that the NMF-driven spectral decomposition is reliable for discriminating physically relevant morphological features from C K EELS SI data of the $IrO_{2-x}$–ionomer composites. However, for $k > 3$, the coefficient maps with small variances exhibited physically irrelevant distributions of intensities, including the noise floor. Thus, the maps sorted as lower-ranked components of $k > 3$ were disregarded because of their morphological irrelevance

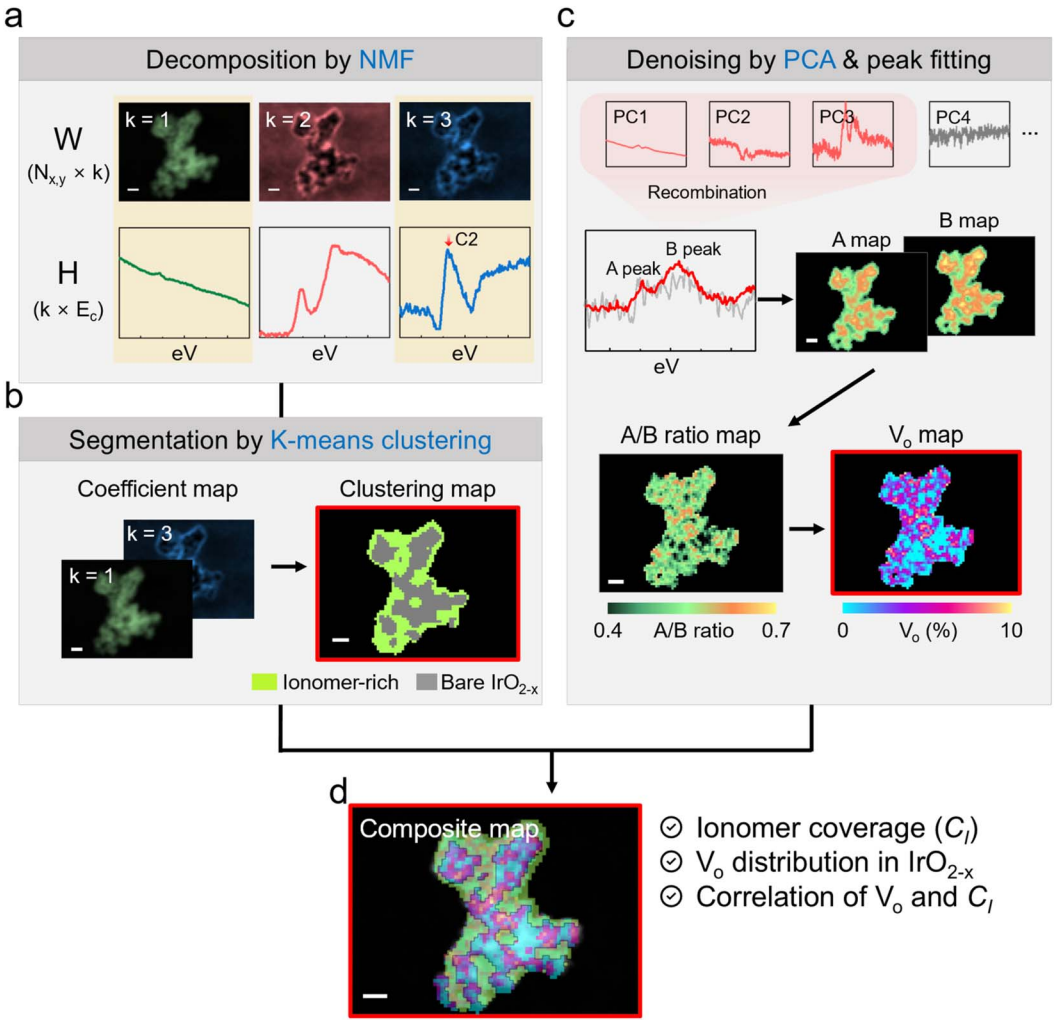


Fig. 5 Clustering and segmentation analysis of C K and O K EELS SI datasets of the $IrO_{2-x}$–ionomer sample. (a) Schematic of the mathematical procedure of matrix conversion and decomposition of the EELS SI data cube (top figures). The first three-ranked coefficient maps and (bottom graphs) the corresponding spectral feature components of the C K EELS SI, decomposed by NMF. (b) Artificial generation of a segmentation map showing the ionomer distribution over the $IrO_{2-x}$ morphology, obtained *via* K-means classification. (c) (Top panels) PCA-driven denoising of O K EELS SI to improve the signal-to-noise ratio and Gaussian peak fitting for generating A and B peak intensity maps. (Bottom panels) Generation of the A/B ratio map and conversion to the $V_o$ distribution map translated by the DFT-driven scaling curve (Fig. 2(b)). (d) Composite map simultaneously representing the spatial distributions of ionomers and $V_o$ inside $IrO_{2-x}$ nanoparticles. The scale bars represent 20 nm.

for interpreting the distribution of the ionomer decorating the $IrO_{2-x}$ particles. It was confirmed that the NMF-driven decomposition of the C K EELS SI reliably separates the ionomer component from the other carbon compounds. However, assessing the ionomer distribution with high accuracy is difficult because the thickness, which affects the EELS intensity, varies across the agglomerated $IrO_{2-x}$–ionomer composite sample. The limitation of 2D projection-based EELS for 3D irregular objects makes quantifying the local content of ionomers distributed over $IrO_{2-x}$ catalysts difficult. In the present geometry, a pixel classified as ionomer-coated may reflect either genuine surface coverage on the top face of an $IrO_{2-x}$ particle or a through-thickness overlap of ionomer and oxide along the beam direction. The impact of these projection artifacts on the statistical conclusions is, however, expected to be limited, as the coverage values represented statistical means derived from more than 70 EELS datasets, thereby reducing the influence of any projection artifact on the ensemble statistics. Hence, as the ionomer coverage on the $IrO_{2-x}$ catalyst particles depends on the ionomer content,[26,60] the 2D EELS map, which visualizes the ionomer coverage, can provide useful information on how the ionomer is morphologically coated on the $IrO_{2-x}$ catalysts. To obtain the ionomer distribution map, we employed an image-segmentation approach based on K-means clustering,[61] which partitions the true EELS signals from the background signals. Thus, each map was classified into two groups of pixels: object (1) and empty space (0) (bottom panels, Fig. 5b).

Second, the experimental O K EELS SI data acquired simultaneously from the same sample region were denoised using the PCA algorithm to enhance the signal-to-noise ratio of the spatially correlated O K-edges (Fig. 5c). In contrast to NMF, PCA imposes no positivity constraints on the ranking of spectral

components of the O K EELS SI data, allowing a bidirectional representation of the spectral data. In this case, negative loadings in the principal components were reported to effectively absorb noise fluctuations (classified as low-variance spectral features) without forcing them into artificial positive signals.[62] Indeed, we confirmed that the truncation of higher-order spectral components ($k \geq 4$) after PCA effectively removes noise fluctuations without creating spurious positive signals, whereas this artificial boosting of an irrelevant weak signal occurs with the application of NMF (Fig. S6). The adaptability and flexibility of PCA are crucial for preserving the authentic shape of O K-edges, allowing reliable evaluation of the A/B peak ratios in the O K-edges. It should be noted that weak signals in the EELS SI data may be filtered by noise components when using PCA. This concern was addressed by optimizing the acquisition conditions to obtain a relatively high-quality EELS SI for the sample protected by a graphene overlayer. After denoising, the reconstructed O K EELS SI was extracted into two intensity maps of the A and B peaks using a Gaussian fitting process to calculate the A/B ratio map, which indirectly represented the local distribution of $V_o$ across the $IrO_{2-x}$ catalyst particles.

As shown in Fig. 2, we observed an increasing trend in the A/B ratio with increasing $V_o$ concentration from the simulated O K-edges. Using this plot as a scaling curve, we translated the measured A/B ratio of the O K fine structure into a variation in the $V_o$ content, thereby directly visualizing the spatial distribution of $V_o$ defects over the $IrO_{2-x}$ catalyst particles (Fig. 5c). Interestingly, the resulting $V_o$ map revealed that iridium oxides with particle sizes of <5 nm were more oxygen-deficient than larger particles (Fig. S7). This result supports previous reports indicating that iridium oxides become increasingly oxygen-deficient as their size decreases because of the multitude of lower-coordinated surfaces and a more flexible lattice that can bear the mixed valence states of iridium atoms.[63,64] By combining this $V_o$ map with the segmented ionomer map, we created an artificial composite map that simultaneously visualized the $V_o$ distribution and ionomer morphology in the iridium oxide catalyst–ionomer composite sample, as shown in Fig. 5d. The resulting composite map allows the evaluation of the ionomer coverage and local $V_o$ content over $IrO_{2-x}$ catalyst particles, which are key parameters in the design and evaluation of PEMWE electrodes. The ionomer coverage ($C_I$) was calculated using the simple relationship $C_I = (A_T - A_E)/A_T$, where $A_T$ and $A_E$ represent the total area of the $IrO_{2-x}$ particles and the exposed area of the $IrO_{2-x}$ particles uncoated by the ionomer, respectively. Because each pixel in the composite image of the $IrO_{2-x}$ particles contains a specific $V_o$ content, the global concentration and local variations of $V_o$ can be simultaneously assessed. However, measurements with a single C K and O K EELS SI dataset may not represent the actual distribution of each electrode component, because of the limited field of observation of the large sample in the high-resolution EELS experiment. To address this concern, a large dataset of C K and O K EELS SI should be prepared and analyzed using the established machine-learning-driven approach, yielding a global landscape for each component distribution with statistical significance.

**Statistical analysis with a large EELS SI dataset**

To obtain statistically meaningful information on the ionomer and $V_o$ distributions across the composite electrode sample, we acquired multiple C K and O K EELS SI datasets ($n > 70$ sets) for random locations on different TEM samples. For each TEM grid, acquisition positions were chosen to represent a range of morphological conditions, including regions with varying particle densities, different degrees of agglomeration, and locations both near and far from the lacey carbon film edges, to minimize systematic spatial bias arising from preferential selection of well-ordered regions. Using the automated machine-learning workflow, rapid clustering and segmentation were performed on a large EELS dataset to generate a series of segmentation maps of $C_I$ and $V_o$ distributions for statistical evaluation (Fig. 6a). After computing every pixel of all the composite maps, we obtained distribution plots that statistically delineated the $C_I$ and $V_o$ over the sample. Fig. 6b shows a histogram of the measured $C_I$ values. The average $C_I$ value was 42.2%, with a measurement variability of 7.3%. Within the $IrO_{2-x}$ particles, the $V_o$ content was measured to be 2.7% $\pm$ 3.2% in total (Fig. 6c). These values fell within the physically reasonable range for $IrO_{2-x}$ synthesized under ambient conditions and were consistent with XPS-based $V_o$ estimates reported for comparable $IrO_{2-x}$ systems,[12,16,20,23] providing indirect support for the reliability of the DFT-calibrated A/B-to-$V_o$ conversion. Given that higher $V_o$ contents were observed in smaller particles, as discussed above, the local variation in the surface charge density induced by the $V_o$ gradient could affect the ionomer–catalyst interface interaction because it is governed by electrostatic forces that control ionomer adsorption on the catalyst surface.[65] Thus, it is anticipated that the ionomer can preferentially adsorb onto a surface region with a relatively high $V_o$ concentration.

To investigate the spatial preference of the ionomer contact depending on the $V_o$ content, we digitally separated the $V_o$ distribution map into two parts of $V_o$ distributions at bare and ionomer-coated $IrO_{2-x}$ particles (denoted as $P_{Vo}$ and $I_{Vo}$, respectively). The left panel in Fig. 6d shows a representative pair of ionomer and $V_o$ distribution maps. Using the ionomer distribution map as a mask filter for the $V_o$ map, the $P_{Vo}$ and $I_{Vo}$ maps were readily computed, as shown in the panels on the right of Fig. 6d. A statistical assessment of the two cases (Fig. 6e) revealed a distinctive bimodal distribution of $V_o$, which differed depending on whether the ionomers contacted the catalyst surface. The measured $V_o$ content in $I_{Vo}$ (6.1% $\pm$ 2.6%) exceeded that in $P_{Vo}$ (4.8% $\pm$ 2.5%). This selective distribution behavior of $V_o$ demonstrates that the electrostatic contact of ionomers on the $IrO_{2-x}$ catalyst surface increases with the increased surface charge density induced by concentrated $V_o$, suggesting a close relationship between the two crucial parameters of $C_I$ and $V_o$ content. With this statistical information describing the degree of inhomogeneity in the ionomer coverage and the $V_o$ concentration within the local regions of the $IrO_{2-x}$–ionomer composite electrode, we can reliably assess the morphological structure of the components in the composite electrode. This information is useful for the development of durable and active

 

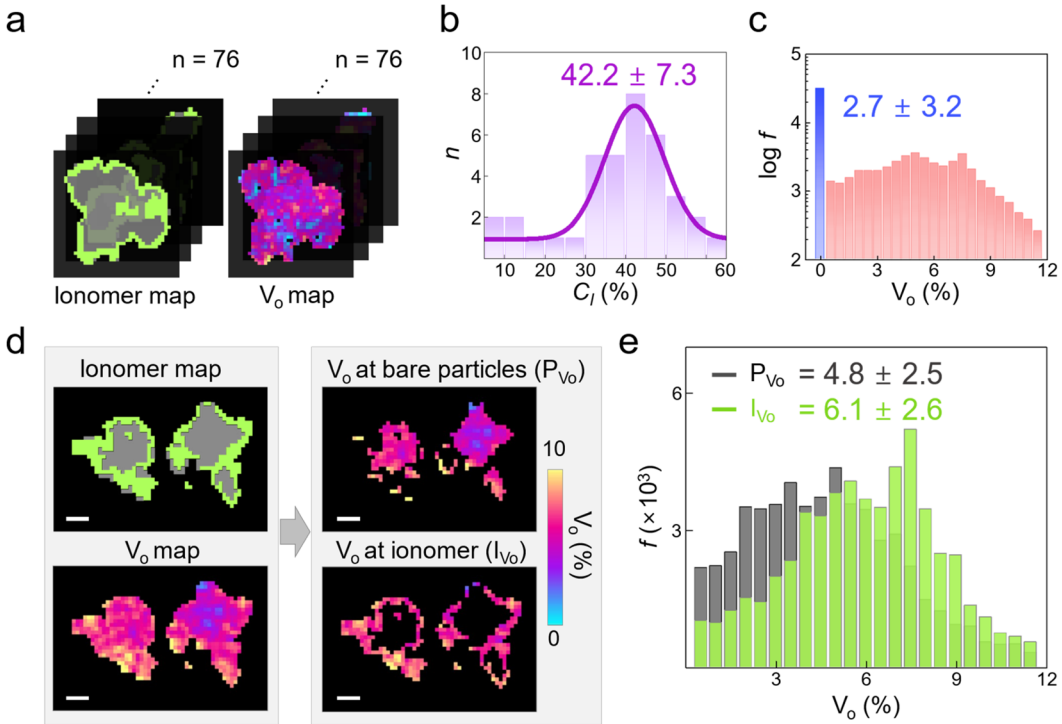


Fig. 6 Statistical analysis of the ionomer coverage ($C_I$) and $V_o$ concentration for the $IrO_{2-x}$–ionomer composite sample. (a) Pairwise series of composite maps showing $C_I$ and $V_o$ distributions. Four pairs of ionomer and $V_o$ maps are representatively displayed among 76 processed maps. (b and c) Histograms of the measured values of $C_I$ and $V_o$ concentration, respectively. The $n$ and $f$ indicate the measured number of $C_I$ and the number of datapoints (or pixels) of $V_o$ values, respectively. (d) Procedure for regional separation of the total $V_o$ distribution in two cases: $P_{Vo}$ and $I_{Vo}$. (e) Histogram of the measured values of $P_{Vo}$ and $I_{Vo}$. The scale bars represent 20 nm.

WE electrodes, as it provides insights into the relationships among catalyst morphology, $V_o$ content, and ionomer coverage.

## Conclusions

We proposed an efficient and reliable chemical-mapping method that leverages a spatially correlated STEM EELS SI technique combined with machine learning to analyze the morphological structure and defect distribution of $IrO_{2-x}$–ionomer nanocomposite electrodes used in PEMWEs. Additionally, we developed a TEM sampling approach and optimized data-acquisition conditions to reduce electron-beam-induced damage to the electrode sample, ensuring high-quality input for the machine-learning algorithms. Using two independent machine-learning models to process the C K and O K EELS data in parallel, we generated chemical maps that reveal the local distribution of $V_o$ and the extent of ionomer coverage without data distortion, which is often caused by manual analysis. More importantly, we demonstrated that the automated processing of a large EELS SI dataset (>70 sets) of the $IrO_{2-x}$–ionomer composite enables the statistically significant evaluation of ionomer coverage and $V_o$ distribution. These findings clarify the overall distribution behavior of $V_o$ and ionomers across the nanocomposite electrode, aiding WE industries and academic researchers in designing high-performance WE electrodes and establishing a benchmark for reliable evaluation. Since this approach can be applied to any oxide catalyst–conducting polymer nanocomposite, we anticipate that it will become a valuable tool for the chemical characterization of sustainable energy conversion materials. The proposed framework is, in principle, extendable to other oxide catalyst–polymer composite systems in which the oxide exhibits a transition metal O K-edge with resolvable $t_{2g}/e_g$ splitting sensitive to vacancy concentration and the polymer contains polar functional groups producing a distinguishable C K-edge feature near ~288 eV. Connecting the nanoscale chemical heterogeneity characterized here to mesoscale morphological parameters, such as electrode porosity, surface area, and electrode–electrolyte contact ratio, represents an important direction for future investigation.

## Author contributions

Yerin Jeon: investigation, validation, software, writing – original draft. Sang-Hyeok Yang: investigation, validation, software, writing – original draft. Hyeon-Ah Ju: investigation, validation, writing – original draft. Kwanhong Park: investigation, software, writing – original draft. Wooseon Choi: investigation. Daehee Yang: investigation. Hakjoo Lee: investigation. Dami Lim: investigation. Shin Jang: resource, investigation. Jaekwang Lee: supervision, software, funding acquisition, writing – review and editing. Jae-Hyeok Kim: supervision, investigation, funding acquisition, writing – review and editing. Young-Min Kim: conceptualization, supervision, investigation, funding acquisition, writing – review and editing.

## Conflicts of interest

The authors declare that they have no competing financial interests or personal relationships that might have influenced the work reported in this study.

## Data availability

The data supporting the findings of this study are available from the corresponding authors upon request.

Supplementary information: Fig. S1: DFT cutoff-energy convergence test; Fig. S2 and Note S1: background-subtraction effect on NMF clustering of C K-edge EELS; Fig. S3: bimodal size distribution of $IrO_{2-x}$ particles; Fig. S4: reference dependence of MLLS fitting; Fig. S5: electron-beam-induced $IrO_{2-x}$-to-Ir phase transition; Fig. S6: PCA *versus* NMF noise removal for O K-edge EELS; Fig. S7: particle-size dependence of the O K-edge A/B ratio; and an Appendix with Python scripts (S1–S3) for STEM-EELS preprocessing, C K-edge phase analysis, and O K-edge oxygen vacancy quantification. See DOI: https://doi.org/10.1039/d5ta08480f.

## Acknowledgements

This study was supported by the National Research Foundation of Korea (NRF) grant (RS-2024-00444986, 50%) funded by the Korean government and the Technology Innovation Program (RS-2024-00433399) funded by the Ministry of Trade, Industry & Energy (MOTIE, Korea). J. L. acknowledges support from the Nano & Materials Technology Development Program through the National Research Foundation of Korea (NRF), funded by the Ministry of Science and ICT (RS-2024-00444649). We acknowledge the support of Hyundai Motor Company.

## Notes and references

1 Y. Ping, G. Galli and W. A. Goddard, III, *J. Phys. Chem. C*, 2015, **119**, 11570–11577.
2 J. Xu, H. Jin, T. Lu, J. Li, Y. Liu, K. Davey, Y. Zheng and S.-Z. Qiao, *Sci. Adv.*, 2023, **9**, eadh1718.
3 H. Zhang, L. Zhu, Y. Shen, M. Wu, T. Tian and H. Tang, *Adv. Compos. Hybrid Mater.*, 2024, **7**, 46.
4 H. Jeon, D. T. Hoang, G. Kim, I. Y. Kim, H. Lee and S. Hong, *Appl. Surf. Sci.*, 2025, **686**, 162088.
5 H. N. Nong, H.-S. Oh, T. Reier, E. Willinger, M.-G. Willinger, V. Petkov, D. Teschner and P. Strasser, *Angew. Chem., Int. Ed.*, 2015, **54**, 2975–2979.
6 J. Feng, F. Lv, W. Zhang, P. Li, K. Wang, C. Yang, B. Wang, Y. Yang, J. Zhou, F. Lin, G.-C. Wang and S. Guo, *Adv. Mater.*, 2017, **29**, 1703798.
7 Y. Lin, Y. Dong, X. Wang and L. Chen, *Adv. Mater.*, 2023, **35**, 2210565.
8 G. Liu, F. Hou, X. Wang and B. Fang, *Appl. Surf. Sci.*, 2023, **615**, 156333.
9 T. X. Zhang, A. L. Coughlin, C.-K. Lu, J. J. Heremans and S. X. Zhang, *J. Phys.: Condens. Matter*, 2024, **36**, 273001.
10 J. Quinson, *Adv. Colloid Interface Sci.*, 2022, **303**, 102643.
11 L. An, C. Wei, M. Lu, H. Liu, Y. Chen, G. G. Scherer, A. C. Fisher, P. Xi, Z. J. Xu and C.-H. Yan, *Adv. Mater.*, 2021, **33**, 2006328.
12 G. Han, J. Y. Kim, K.-J. Kim, H. Lee and Y.-M. Kim, *Appl. Surf. Sci.*, 2020, **507**, 144916.
13 Y.-H. Kim, S. Kim, K.-j. Kim, C. Kim, J. H. Jang, Y.-M. Kim and H. Lee, *J. Mater. Chem. A*, 2020, **8**, 25345–25354.
14 O. Kwon, Y. I. Kim, K. Kim, J. C. Kim, J. H. Lee, S. S. Park, J. W. Han, Y.-M. Kim, G. Kim and H. Y. Jeong, *Nano Lett.*, 2020, **20**, 8353–8359.
15 Y. I. Kim, M. Jeong, J. Byun, S.-H. Yang, W. Choi, W.-S. Jang, J. Jang, K. Lee, Y. Kim, J. Lee, E. Lee and Y.-M. Kim, *Mater. Today Phys.*, 2021, **16**, 100302.
16 W.-S. Jang, Y. Jin, Y.-H. Kim, S.-H. Yang, S. J. Kim, J. A. Hong, J. Baik, J. Lee, H. Lee and Y.-M. Kim, *Appl. Catal., B*, 2022, **305**, 121083.
17 W.-S. Jang, V. N. Pham, S.-H. Yang, J. Baik, H. Lee and Y.-M. Kim, *Appl. Catal., B*, 2023, **322**, 122140.
18 C. Cai, S. Han and Y. Tang, *Sustainable Energy Fuels*, 2020, **4**, 2462–2468.
19 E. A. Carbonio, F. Sulzmann, D. Teschner, J. J. Velasco-Vélez, M. Hävecker, A. K. Gericke, R. Schlögl and T. Jones, *Catal. Sci. Technol.*, 2024, **14**, 572–580.
20 R. Guo, J. Wang, J. Li, H. Li, H. Wang, Y. Cao, J. Chen, T. Cheng, H. Yang and M. Sheng, *ACS Catal.*, 2024, **14**, 11164–11171.
21 Y. Wu, C. Guo, R. Yao, K. Zhang, J. Li and G. Liu, *Adv. Funct. Mater.*, 2024, **34**, 2410193.
22 C. Kong, C. Zhi, Z. Wu, W. Yang, J. Yang and Z. Sun, *J. Colloid Interface Sci.*, 2024, **665**, 863–870.
23 L. Zhang, N. Zhang, H. Shang, Z. Sun, Z. Wei, J. Wang, Y. Lei, X. Wang, D. Wang, Y. Zhao, Z. Sun, F. Zhang, X. Xiang, B. Zhang and W. Chen, *Nat. Commun.*, 2024, **15**, 9440.
24 Y.-M. Kim, J. He, M. D. Biegalski, H. Ambaye, V. Lauter, H. M. Christen, S. T. Pantelides, S. J. Pennycook, S. V. Kalinin and A. Y. Borisevich, *Nat. Mater.*, 2012, **11**, 888–894.
25 H.-A. Ju, E.-B. Park, J. Hwang, Y.-H. Kim, M.-H. Jung, M.-J. Yang, S. J. Kim, J. Lee, I. Kim, Y.-S. Kim, S. Yoon, J. H. Jang, H. Y. Jeong, J. Lee, J.-H. Shim and Y.-M. Kim, *ACS Energy Lett.*, 2024, **9**, 5606–5615.
26 A. Y. Borisevich, A. N. Morozovska, Y.-M. Kim, D. Leonard, M. P. Oxley, M. D. Biegalski, E. A. Eliseev and S. V. Kalinin, *Phys. Rev. Lett.*, 2012, **109**, 065702.
27 N. Kakati, L. Anderson, G. Li, D. M. Sua-an, A. Karmakar, J. D. Ocon and P.-Y. A. Chuang, *ACS Appl. Mater. Interfaces*, 2023, **15**, 55559–55569.
28 W. Xu and K. Scott, *Int. J. Hydrogen Energy*, 2010, **35**, 12029–12037.
29 M. Bernt and H. A. Gasteiger, *J. Electrochem. Soc.*, 2016, **163**, F3179.
30 A. Y. Faid, L. Xie, A. O. Barnett, F. Seland, D. Kirk and S. Sunde, *Int. J. Hydrogen Energy*, 2020, **45**, 28272–28284.
31 G. Huang, M. Mandal, N. U. Hassan, K. Groenhout, A. Dobbs, W. E. Mustain and P. A. Kohl, *J. Electrochem. Soc.*, 2021, **168**, 024503.

 

32 H. J. Lee, S. Choe, D. Shin, I. Jeong, S. K. Cho, S. J. Yoo, J. Y. Kim, K. H. Lim, S. Y. Lee, H. S. Park, K. H. Song, J. H. Jang and H. Y. Park, *Korean J. Chem. Eng.*, 2025, **42**, 71–79.
33 S.-H. Yang, E.-B. Park, S. Y. Cho, Y. S. Kang, H.-A. Ju, Y. Jeon, D. Yang, S.-D. Yim, S. Lee and Y.-M. Kim, *Mater. Today Energy*, 2023, **36**, 101348.
34 S. P. Gleason, D. Lu and J. Ciston, *npj Comput. Mater.*, 2024, **10**, 221.
35 H.-A. Ju, D. Thanh Hoang, W.-S. Jang, Y.-H. Kim, E.-B. Park, S.-H. Yang, K. Ihm, J. Hyuck Jang, Y.-M. Kim and H. Lee, *Appl. Surf. Sci.*, 2025, **679**, 161197.
36 J.-H. Shim, H. Kang, Y.-M. Kim and S. Lee, *ACS Appl. Mater. Interfaces*, 2019, **11**, 44293–44299.
37 P. Pujar, H. Cho, Y.-H. Kim, N. Zagni, J. Oh, E. Lee, S. Gandla, P. Nukala, Y.-M. Kim, M. A. Alam and S. Kim, *ACS Nano*, 2023, **17**, 19076–19086.
38 S. Kang, W.-S. Jang, A. N. Morozovska, O. Kwon, Y. Jin, Y.-H. Kim, H. Bae, C. Wang, S.-H. Yang, A. Belianinov, S. Randolph, E. A. Eliseev, L. Collins, Y. Park, S. Jo, M.-H. Jung, K.-J. Go, H. W. Cho, S.-Y. Choi, J. H. Jang, S. Kim, H. Y. Jeong, J. Lee, O. S. Ovchinnikova, J. Heo, S. V. Kalinin, Y.-M. Kim and Y. Kim, *Science*, 2022, **376**, 731–738.
39 G. Kresse and D. Joubert, *Phys. Rev. B*, 1999, **59**, 1758–1775.
40 G. Kresse and J. Furthmüller, *Phys. Rev. B*, 1996, **54**, 11169–11186.
41 J. P. Perdew, A. Ruzsinszky, G. I. Csonka, O. A. Vydrov, G. E. Scuseria, L. A. Constantin, X. Zhou and K. Burke, *Phys. Rev. Lett.*, 2008, **100**, 136406.
42 P. E. Blöchl, O. Jepsen and O. K. Andersen, *Phys. Rev. B*, 1994, **49**, 16223–16233.
43 F. Karsai, M. Humer, E. Flage-Larsen, P. Blaha and G. Kresse, *Phys. Rev. B*, 2018, **98**, 235205.
44 D. D. Lee and H. S. Seung, *Nature*, 1999, **401**, 788–791.
45 Z. B. Yan, R. Hayes, L. G. A. Melo, G. R. Goward and A. P. Hitchcock, *J. Phys. Chem. C*, 2018, **122**, 3233–3244.
46 Y.-M. Kim, S. B. Lee, J. Lee and S. H. Oh, *Nanoscale*, 2019, **11**, 8281–8292.
47 A. Y. Borisevich, H. J. Chang, M. Huijben, M. P. Oxley, S. Okamoto, M. K. Niranjan, J. D. Burton, E. Y. Tsymbal, Y. H. Chu, P. Yu, R. Ramesh, S. V. Kalinin and S. J. Pennycook, *Phys. Rev. Lett.*, 2010, **105**, 087204.
48 F. Scarpelli, N. Godbert, A. Crispini and I. Aiello, *Inorganics*, 2022, **10**, 115.
49 M. V. Ganduglia-Pirovano, A. Hofmann and J. Sauer, *Surf. Sci. Rep.*, 2007, **62**, 219–270.
50 K. Schweinar, B. Gault, I. Mouton and O. Kasian, *J. Phys. Chem. Lett.*, 2020, **11**, 5008–5014.
51 D. Escalera-López, S. Czioska, J. Geppert, A. Boubnov, P. Röse, E. Saraçi, U. Krewer, J.-D. Grunwaldt and S. Cherevko, *ACS Catal.*, 2021, **11**, 9300–9316.
52 H. M. Tsai, P. D. Babu, C. W. Pao, J. W. Chiou, J. C. Jan, K. P. Krishna Kumar, F. Z. Chien, W. F. Pong, M.-H. Tsai, C.-H. Chen, L. Y. Jang, J. F. Lee, R. S. Chen, Y. S. Huang and D. S. Tsai, *Appl. Phys. Lett.*, 2007, **90**, 042108.
53 T.-D. Tran and D. Ozkaya, *BIO Web Conf.*, 2024, **129**, 25004.
54 F. Pedregosa, G. Varoquaux, A. Gramfort, V. Michel, B. Thirion, O. Grisel, M. Blondel, P. Prettenhofer, R. Weiss, V. Dubourg, J. Vanderplas, A. Passos, D. Cournapeau, M. Brucher, M. Perrot and É. Duchesnay, *J. Mach. Learn. Res.*, 2011, **12**, 2825–2830.
55 J. Ryu, H. Kim, R. M. Kim, S. Kim, J. Jo, S. Lee, K. T. Nam, Y.-C. Joo, G.-C. Yi, J. Lee and M. Kim, *Ultramicroscopy*, 2021, **231**, 113314.
56 L. Yedra, E. Xuriguera, M. Estrader, A. López-Ortega, M. D. Baró, J. Nogués, M. Roldan, M. Varela, S. Estradé and F. Peiró, *Microsc. Microanal.*, 2014, **20**, 698–705.
57 S. Guo, H. Yun, S. Nair, B. Jalan and K. A. Mkhoyan, *Nat. Commun.*, 2023, **14**, 6005.
58 R. Zan, Q. M. Ramasse, R. Jalil, T. Georgiou, U. Bangert and K. S. Novoselov, *ACS Nano*, 2013, **7**, 10167–10174.
59 J. M. Yuk, J. Park, P. Ercius, K. Kim, D. J. Hellebusch, M. F. Crommie, J. Y. Lee, A. Zettl and A. P. Alivisatos, *Science*, 2012, **336**, 61–64.
60 Y. S. Park, M. J. Jang, J.-Y. Jeong, J. Lee, J. Jeong, C. Kim, J. Yang and S. M. Choi, *Int. J. Energy Res.*, 2023, **2023**, 3764096.
61 A. Likas, N. Vlassis and J. J. Verbeek, *Pattern Recognit.*, 2003, **36**, 451–461.
62 S. Lichtert and J. Verbeeck, *Ultramicroscopy*, 2013, **125**, 35–42.
63 J. Xu, L. Chang, Y. Wei, J. Wei, W. Cui, Y. Tao and L. Gan, *ACS Nano*, 2024, **18**, 29140–29151.
64 Z. Yu, J. Xu, Y. Li, B. Wei, N. Zhang, Y. Li, O. Bondarchuk, H. Miao, A. Araujo, Z. Wang, J. L. Faria, Y. Liu and L. Liu, *J. Mater. Chem. A*, 2020, **8**, 24743–24751.
65 S. A. Berlinger, B. D. McCloskey and A. Z. Weber, *ACS Energy Lett.*, 2021, **6**, 2275–2282.